



A CFD-Based Study of the Feasibility of Adapting an Erosion Burner Rig for Examining the Effect of CMAS Deposition/Corrosion on Environmental Barrier Coatings

*Robert A. Miller and Maria A. Kuczmariski
Glenn Research Center, Cleveland, Ohio*

NASA STI Program . . . in Profile

Since its founding, NASA has been dedicated to the advancement of aeronautics and space science. The NASA Scientific and Technical Information (STI) Program plays a key part in helping NASA maintain this important role.

The NASA STI Program operates under the auspices of the Agency Chief Information Officer. It collects, organizes, provides for archiving, and disseminates NASA's STI. The NASA STI Program provides access to the NASA Technical Report Server—Registered (NTRS Reg) and NASA Technical Report Server—Public (NTRS) thus providing one of the largest collections of aeronautical and space science STI in the world. Results are published in both non-NASA channels and by NASA in the NASA STI Report Series, which includes the following report types:

- TECHNICAL PUBLICATION. Reports of completed research or a major significant phase of research that present the results of NASA programs and include extensive data or theoretical analysis. Includes compilations of significant scientific and technical data and information deemed to be of continuing reference value. NASA counter-part of peer-reviewed formal professional papers, but has less stringent limitations on manuscript length and extent of graphic presentations.
- TECHNICAL MEMORANDUM. Scientific and technical findings that are preliminary or of specialized interest, e.g., “quick-release” reports, working papers, and bibliographies that contain minimal annotation. Does not contain extensive analysis.
- CONTRACTOR REPORT. Scientific and technical findings by NASA-sponsored contractors and grantees.
- CONFERENCE PUBLICATION. Collected papers from scientific and technical conferences, symposia, seminars, or other meetings sponsored or co-sponsored by NASA.
- SPECIAL PUBLICATION. Scientific, technical, or historical information from NASA programs, projects, and missions, often concerned with subjects having substantial public interest.
- TECHNICAL TRANSLATION. English-language translations of foreign scientific and technical material pertinent to NASA's mission.

For more information about the NASA STI program, see the following:

- Access the NASA STI program home page at <http://www.sti.nasa.gov>
- E-mail your question to help@sti.nasa.gov
- Fax your question to the NASA STI Information Desk at 757-864-6500
- Telephone the NASA STI Information Desk at 757-864-9658
- Write to:
NASA STI Program
Mail Stop 148
NASA Langley Research Center
Hampton, VA 23681-2199



A CFD-Based Study of the Feasibility of Adapting an Erosion Burner Rig for Examining the Effect of CMAS Deposition/Corrosion on Environmental Barrier Coatings

*Robert A. Miller and Maria A. Kuczmariski
Glenn Research Center, Cleveland, Ohio*

National Aeronautics and
Space Administration

Glenn Research Center
Cleveland, Ohio 44135

Trade names and trademarks are used in this report for identification only. Their usage does not constitute an official endorsement, either expressed or implied, by the National Aeronautics and Space Administration.

Level of Review: This material has been technically reviewed by technical management.

Available from

NASA STI Program
Mail Stop 148
NASA Langley Research Center
Hampton, VA 23681-2199

National Technical Information Service
5285 Port Royal Road
Springfield, VA 22161
703-605-6000

This report is available in electronic form at <http://www.sti.nasa.gov/> and <http://ntrs.nasa.gov/>

A CFD-Based Study of the Feasibility of Adapting an Erosion Burner Rig for Examining the Effect of CMAS Deposition/Corrosion on Environmental Barrier Coatings

Robert A. Miller and Maria A. Kuczmarzski
National Aeronautics and Space Administration
Glenn Research Center
Cleveland, Ohio 44135

Abstract

Thermodynamic and computational fluid dynamics modeling has been conducted to examine the feasibility of adapting the NASA Glenn erosion burner rigs for use in studies of corrosion of environmental barrier coatings by the deposition of molten CMAS. The effect of burner temperature, Mach number, particle preheat, duct heating, particle size, and particle phase (crystalline vs. glass) were analyzed. Detailed strategies for achieving complete melting of CMAS particles were developed, thereby greatly improving the probability of future successful experimental outcomes.

Introduction

Thermal barrier coatings (TBCs) insulate air cooled superalloy components in the hot gas path of gas turbine engines. They allow higher gas temperatures and lower cooling air flows resulting in improved engine efficiency than would be possible with uncoated components. However, TBC upper use temperatures are limited by durability concerns. For example, the upper surface temperature of current TBCs on high pressure turbine airfoils is intentionally kept below approximately 1473 K (1200 °C; 2190 °F), which is below the melting point of a common environmental contaminant, essentially ingested dust, known as calcium magnesium aluminosilicate (CMAS) [Darolia, 2013]. Ingested CMAS can melt in the combustor and deposit on the surface of the turbine airfoils. If the coating surface temperature is allowed to rise to above the melting point of the particular deposited CMAS, then the CMAS can wick into the porous coating reducing the strain tolerance or corrosively attacking it. Such concerns may limit acceptance of new low conductivity TBCs [Darolia, 2013], even though they may be otherwise be capable of operation at surface temperatures above 1473 K (1200 °C; 2190 °F).

Environmental barrier coatings (EBCs) for silicon carbide-based ceramic matrix composites (CMCs) may also require future use at temperatures above 1473 K. EBC-coated CMCs are leading candidates to replace turbine section superalloy components because they are capable of higher temperature operation, weigh less, and, in some applications, may not even require air cooling. However, EBCs are also subject to CMAS deposition, infiltration, and attack. If EBC coated CMCs are to be completely viable as replacement materials for TBC-coated superalloys, the upper surface temperature of the ceramic must be allowed to operate at temperatures above the 1473 K melting point of CMAS. A typical composition of a low melting CMAS, discounting minor amounts of transition metal oxides, is: 35 mol% CaO, 10 mol% MgO, 7 mol% Al₂O₃, 48 mol% SiO₂. Melting temperatures for this composition are variously reported as 1500 or 1513 K (1227 or 1240 °C, 2240 or 2264 °F) [Darolia, 2007; 2013]. In addition to melting temperature, CMAS compositions, including CMAS-based slags and fly ash, are characterized by two other temperatures: softening and fluidity points as defined by standard cone tests (ASTM 2010). For example, a slag with a similar melting point to the CMAS described above had softening temperature 95 K or °C (171 °F) below the melting temperature and fluidity temperature 10 K or °C (18 °F) above the

melting temperature [Vassilev, 1995]. As mentioned above, molten CMAS particles that deposit on TBCs or EBCs are very corrosive when the ceramic coating is above the melting point of the CMAS (and perhaps especially if it is above its fluidity point). Unmelted CMAS particles can cause solid particle erosion, although, presumably, solid CMAS particles with temperatures above the softening point may not be as erosive as particles at temperatures below the softening point. However, this has not yet been experimentally verified.

Current techniques for evaluating CMAS corrosion of coatings rely on pre-application of CMAS using techniques such as aqueous suspensions or pastes followed by heating, which is most often conducted using a furnace. A more realistic approach would be to develop a test where CMAS is gradually deposited during cyclic burner rig testing. An unattached-ducted burner rig—which is presently used at NASA to study solid particle erosion [Kuczmariski, 2011; Miller, 2011; Miller, 2013]—is being considered for CMAS erosion/deposition/corrosion studies. Figure 1(a) shows the schematic for a burner rig that feeds the unattached duct shown in Figure 1(b). As currently configured, alumina grit erodent is typically injected into the flame. CFD modeling showed that fine alumina grit (20 μm , although labeled 26 μm in the paper) injected into a 1644 K burner heats up to a temperature that is close to the melting point of CMAS. The upper temperature of the particles was believed to approach the static temperature of the gas because that is the temperature that a particle traveling at the gas velocity would experience. In other words, for the limiting case of zero slip velocity, the particle temperature will approach the static temperature. This ignores a correction for radiation losses that would lead to lower particle temperature. This correction may mainly be important as the particle approaches the velocity and the static temperature of the gas, at which point the very high heat transfer from the gas to the small particle drops to values more in line with the heat transfer from radiative cooling. As mentioned above, previous efforts focused on alumina erodents. If it can be demonstrated that injected CMAS particles can be made to melt in this rig, it may be feasible to use it to study CMAS erosion/deposition/corrosion and to evaluate CMAS resistant coatings under more realistic conditions than usual laboratory furnace tests.

A preliminary CFD study was conducted for this paper to determine whether it would be feasible to melt CMAS particles in the ducted NASA burner rig and to understand how to best operate the burner to maximize the chances that melting has been achieved. A CFD model, reported previously [Kuczmariski 2011; Miller 2011, 2013], was used for this study. CMAS particle tracks were modeled using a turbulent dispersion model with 20 tracks each representing 20, 30, and 40 μm diameter particles, respectively. Ten different injection points and three different injection velocities were modeled. However, for clarity, the results from two injection points and one injection velocity are plotted in most examples. Transport properties of the gas phase for this initial study were approximated by using the properties for air. This is expected to result in somewhat conservative predictions for particle heating. Thermodynamic properties

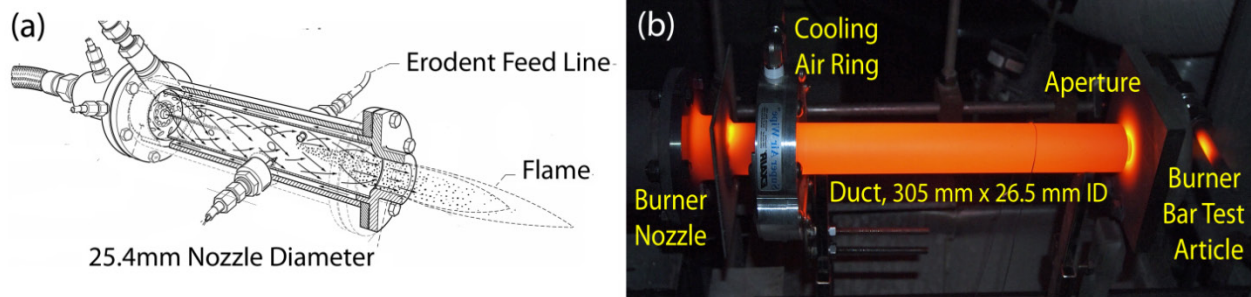


Figure 1.—Erosion burner rig with unattached-duct

for the CMAS composition specified above were estimated from rule-of-mixtures averages of the tabulated properties [Chase, 1998] of the individual component oxides as recommended in the literature [Mills, 2011]. These properties included solid and liquid phase heat capacities and entropies. For CMAS in the form of a glass, a rule-of-mixtures average of the constant high temperature values for the liquid heat capacities were used to represent the heat capacity of glass CMAS at all temperatures. Additionally, the tabulated entropies were used to obtain rule-of-mixtures entropies for the liquid and solid phases. The heat of melting was taken as $T_m\Delta S$ [Mills, 2011], where T_m is the assumed CMAS melting point taken as 1500 K; the ΔS term is the change in entropy between the tabulated solid and liquid phases at T_m . The heat of melting, which was required for modeling the case of a crystalline CMAS, was inputted into the CFD software as an additional heat capacity over the range of 1500 to 1520 K. That is, the rule-of-mixtures value of 330,000 J/kg was expressed as an additional heat capacity of 16,500 J/kg-K between 1500 and 1520 K. The CMAS density was obtained using the rule-of-mixtures average of the molar volumes. The molecular weights of the individual components of CMAS were used to convert room temperature molar volumes to obtain a density of 2800 kg/m³. No attempt was made to correct for the changes in density with temperature or due to phase change. For the case of a glass phase CMAS, where the heat capacity of the liquid were used over all temperatures, the heat of melting does not apply because it was treated as a supercooled liquid.

The heat capacities-versus-temperature curves may be integrated to produce curves of enthalpy versus temperature. For the case of a fully crystalline CMAS, the enthalpy rises smoothly until the material reaches the melting range, then rises an additional amount governed by the heat of melting. The enthalpy curve continues in the liquid phase at a different slope based on the value assumed for the heat capacity of the liquid. This behavior is observed in the lower, black line on Figure 2. For the case where the particles begin as a glass, the plot of enthalpy versus temperatures is linear because of the constant value assumed for the heat capacity; this is the upper, red line below. These two curves are expected to come to the same value at the melting point [Mills, 2011] and they nearly do so—agreeing within 6%—even though they were estimated independently. Figure 4 of the paper by Mills suggests that the heat capacity of glass CMAS at temperatures below the melting point may be somewhat lower than the constant temperature value found above the melting point. A small adjustment could have been made to bring the enthalpies for crystalline and glass CMAS together at the melting point, but a decision was made to accept the high temperature constant value as an upper limit for the heat capacity of the glass.

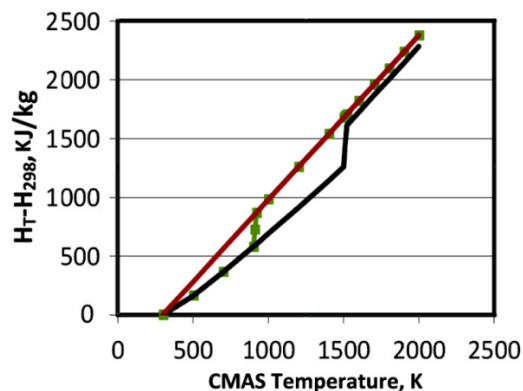


Figure 2.—Plot of enthalpy versus temperature derived from the thermodynamic properties used for the CFD modeling for crystalline (lower black line) or glass CMAS particles (upper red line) or particles that transform from crystalline to glass (lines with symbols). The enthalpies at higher temperatures calculated independently agree within 6% at the melting temperature.

The case where the CMAS is crystalline at low temperatures but undergoes a transition to the glass phase at a glass transition temperature, T_g , was also examined. This case may be more representative of the behavior of CMAS-based slags in steel mills. The enthalpy for this case is represented on the plot by the green line with green squares. With this model, the curve for the crystalline phase is followed until the glass transition temperature, taken here as 900 K, is reached, at which point it transitions to the enthalpy curve for the glass phase. The value of the ΔH_{glass} was adjusted to match the enthalpy for the glass at the melting point (as well as all points above T_g). Similar to the approach used for the crystalline case, the ΔH_{glass} was treated as an additional heat capacity equal to ΔH_{glass} divided by 20 in the range of 900 to 920 K. The results for this case will not be shown because they are nearly indistinguishable from the case where the particles are assumed to be in the glass phase beginning at room temperature.

The burner temperature, or the equivalent temperature of the isentropic core of the flame, had been reported as 1644 K (1371 °C, 2500 °F) using uncorrected, bare thermocouples [Erturk, 1995; D. Zhu, NASA, personal communication, 2007 and 2013]. However, a Type R thermocouple in the isentropic core of a burner was recently observed to read higher than 2030 K (1760 °C, 3200 °F), which is above the reliable upper usable temperature of Type R thermocouples [M Cuy, NASA, personal communication, 2013]. The bead and both legs of the thermocouple appeared to suffer incipient melting, which suggests that the flame could have been over 2110 K (1840 °C, 3340 °F) based on the phase diagram [Okamoto 2013]. In another NASA rig, the ducted burner erosion rig, the nozzle exit temperature was found to be over 2000 K and the temperature at the duct exit was found to be only a few tens of degrees lower than the temperature at the nozzle exit. The duct wall temperature at mid-length was found to be over 1200 K and the difference between the gas temperature and the temperature of the duct wall increased as the gas temperature increased. This behavior would be expected if the duct wall was being cooled by radiation and convection to its surroundings. At another laboratory, a similarly high burner temperature of 1923 K (1650 °C, 3000 °F) was reported [Immarigeon, 1997]. Therefore, for the present study, the effect of burner temperature was modeled by examining both 1644 K and a 300 K hotter burner at 1944 K. The two temperatures are expected to have a relatively small effect on gas velocity because the ratio of the sonic velocities for the two temperatures is only 1.08, which is equal to the square root of the temperature ratio. However, when we are concerned with melting, temperature will be a prime consideration.

Results

Modeled CMAS particle temperatures were plotted versus distance from particle injection. Nozzle exit location on the plot is at 0.111125 m. The duct exit was at 0.428626 m. These two exit locations will be indicated by diamond symbols on the plots of temperature versus distance from injection that follow. An aperture, which had been used in the previous study, was positioned 0.0508 m from the end of the duct and a specimen at 0.0254 m after the aperture. Particles were modeled to be captured by the aperture plate and specimen. The specimen, aperture and duct were modeled to radiatively cool with an emissivity of 1.00. The curves terminate at the specimen distance. Particles that did not pass through the aperture were seen to decrease in temperature as they interacted with the aperture wall. Many of the particles that did not pass through the aperture are not traveling parallel to the duct. The aperture prevents those particles from reaching the substrate.

The plots in Figure 3(a) to (d) show temperature versus distance from injection of the particle tracks for 20, 30 and 40 μm crystalline particles associated with the upper, middle, and lower family of curves, respectively, on each plot. Figure 3(a) and (c) represent Mach 0.5 rig operation, and Figure 3(b) and (d) represent Mach 0.3. Figure 3(a) and (b) represent 1644 K burner temperature, and Figure 3(c) and (d) are

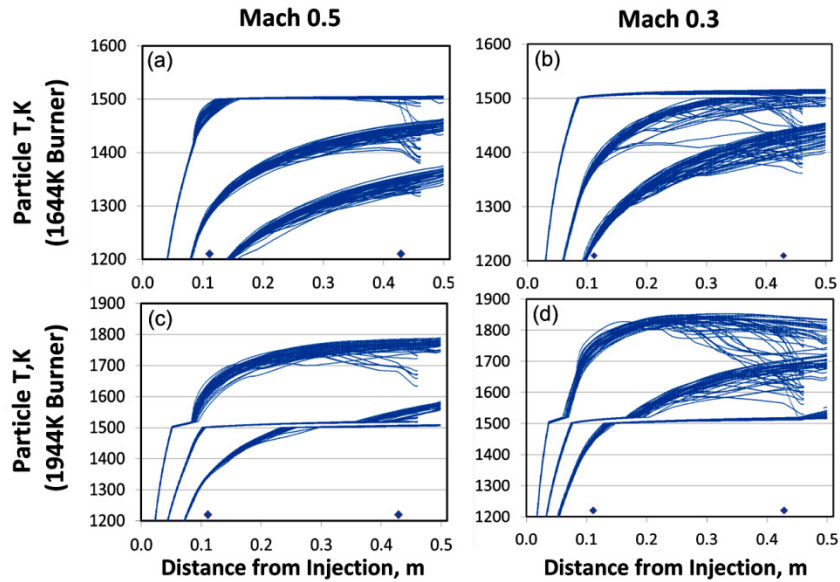


Figure 3.—Modeled particle temperature versus distance from injection for CMAS particles of diameter 20 μm (upper family of curves), 30 μm (middle family), or 40 μm (lower family) for burner temperatures of 1644 and 1944 K and Mach numbers of 0.5 and 0.3. Diamond shaped symbols represent burner and duct exit locations, respectively.

for 1944 K. In each case, the particles were seen to heat up, with most of the temperature rise occurring within the burner. The particles continued to heat up after exiting the burner (i.e., beyond 0.111125 m), although the temperature increased at a slower rate. As expected for crystalline particles, the particle temperatures remained at the melting point (i.e., at the assumed 1500 to 1520 K melting range) and do not continue to rise until the entire particle has melted. The initiation of melting is favored by smaller particle size (20 vs. 40 μm in each figure), higher burner temperature (Figure 3(c) vs. (a) and Figure 3(d) vs. (b)), and lower Mach number (Figure 3(b) vs. (a) and Figure 3(d) vs. (c)). The beneficial effect of lower Mach number assumed that the Mach 0.3 burner comes to essentially the same burner temperature as the Mach 0.5 burner. This assumption is supported by thermodynamic calculations using the NASA chemical equilibrium code [McBride, 2002], which show a drop of less than 3 K drop in adiabatic temperature in going from the burner pressure required for Mach 0.5 to the pressure for Mach 0.3. None of the particles had completely melted in the 1644 K burner case (Figure 3(a) and 3 (b)), although the 20 μm particles were partially melted. In the 1944 K burner (Figure 3(c) and (d)), the 20 and 30 μm and particles had completely melted and their temperatures continued to rise after melting. In the Mach 0.3 case (Figure 3(d)) the completely melted particles rose to essentially the static temperature of the gas, and then began to fall as the static temperature fell. The 40 μm particles were partially melted in the 1944 K Mach 0.5 case (Figure 3(c)) and were completely melted in the Mach 0.3 case (Figure 3(d)).

Figure 4(a) to (c) represents the particle tracks for the 20, 30, and 40 μm crystalline particles in the 1644 K, Mach 0.3 burner rig. Figure 4(a) is repeated from Figure 3(b). Figure 4(b) examines the effect of preheating the particles by 400 K which is a temperature that should be easily achievable using heating cables. A small benefit in final particle temperatures was observed. Figure 4(c) represents the case where the particles had been preheated and the duct had been heated to 1473 K. This is a temperature achievable using an advanced superalloy in a tube furnace. An additional small benefit in final particle temperature was observed from the preheated duct and now the 20 μm particles had completely melted near the duct exit. The heated duct also led to a noticeable narrowing of the spread of curves for each particle size.

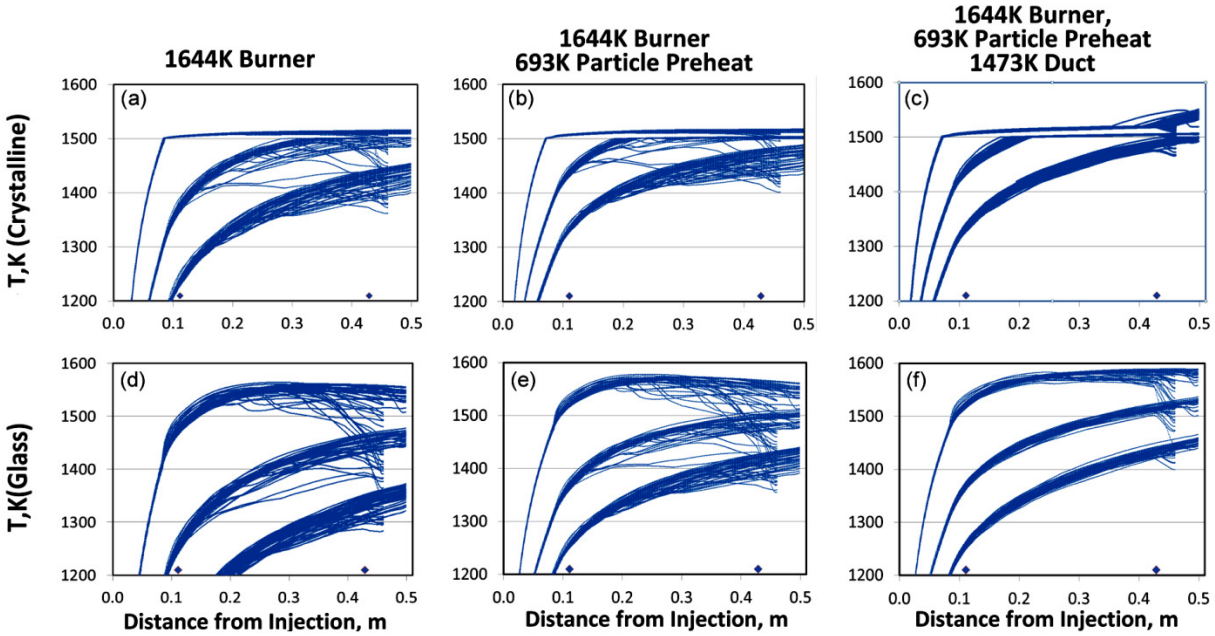


Figure 4.—Modeled particle temperature versus distance from injection for CMAS particles of diameter 20 μm (upper family of curves on each plot), 30 μm (middle family), or 40 μm (lower family) for 1644 K burner temperature and Mach 0.3 with and without particle preheating and duct heating. Diamond shaped symbols represent burner and duct exit locations, respectively.

Because particle temperatures continued to increase with distance by the end of the duct, there may be a benefit to lengthening the duct. In that case, there likely would be a benefit of heating a lengthened duct to counteract the expected drop in total temperature. To summarize, the first-order solution for achieving complete particle melting for cases where the burner temperature is limited to 1644 K is to operate at Mach 0.3 and to decrease the particle size to 20 μm . Small additional benefits can be obtained by preheating the particles and heating the duct.

Figure 4(a) to (c) represent the heating curves for particles that were initially in the glass phase. Based on the plot of enthalpy versus temperature shown in Figure 2, more energy was required to heat the glass particles up to just before their melting point. However, there was no additional heat of melting required to melt the particles because glass is essentially a supercooled liquid. As a result, the 30 and 40 μm particles never reached the melting point and came to a lower final temperature for the 1644 K burner case. However, the 20 μm glass particles came to a higher final temperature because their temperature does not stall at the melting point. As with the case where the particles were crystalline, the spread of temperatures for each particle size was narrower when the duct is used.

The next set of plots in Figure 5 show 20, 30, and 40 μm particles that are heating in a rig operated at Mach 0.3 with a 1944 K burner temperature. Figure 5(a) to (c) represent crystalline particles and Figure 5(d) to (f) represent glass particles. Figure 5(a) represents the crystalline particle case where there is no preheating of the particle or duct. The upper two tracks in that figure for 20 and 30 μm particles, respectively, had completely melted, and the 20 μm particles appeared to come to the static temperature of the gas. Most of the 40 μm particles, in the lower set of tracks, were incompletely melted. Preheating the particles, Figure 5(b), had a small effect on the 20 and 30 μm particles (in the upper two sets of tracks). However, the 40 μm particles (in the lower set of tracks) had now completely melted just before reaching the specimens. Of course, uncertainties in the analysis would prevent one from relying on the result that the melting is complete. Preheating the duct, Figure 5(c), leads to somewhat higher particle

temperatures with a somewhat narrower spread of particle tracks. The 40 μm particles in the lower set of curves were now predicted to melt before the duct exit (which is represented by the second diamond symbol on the plot). In principle, the duct could be heated to a higher temperature with additional benefit if it was made of a ceramic material. A 19 mm internal-diameter mullite duct was placed inside of a larger metal duct and used briefly in experiments reported earlier. [Miller, 2011] However, there are durability concerns for using a ceramic duct. An insulated silicon carbide duct was used for deposition studies of fly ash from gas temperatures up to 1561 K (1288 $^{\circ}\text{C}$, 2350 $^{\circ}\text{F}$) [Laycock, 2013]. Deposits were observed on the walls of the silicon carbide duct; deposits were not observed in an earlier version of their rig which used a superalloy duct. Deposits were observed on metallic test articles having initial surface temperatures between about 1363 K (1090 $^{\circ}\text{C}$, 1994 $^{\circ}\text{F}$) and 1408 K (1135 $^{\circ}\text{C}$, 2075 $^{\circ}\text{F}$). Their fly ash mean diameters were 3 or 13 μm .

In another study, fly ash deposits were found on the metallic test section in a high temperature combustion facility having reported gas temperatures of up to 1560 K (1287 $^{\circ}\text{C}$, 2348 $^{\circ}\text{F}$) [Murphy, 2013]. In this study the mean particle size of the fly ash was 13 μm , the pressure was approximately 4 bar, and the gas velocity was 66 m/sec. Deposits were observed on the surface of TBC coated test articles having backside temperature of up to 991 K (718 $^{\circ}\text{C}$, 1324 $^{\circ}\text{F}$) when the gas temperature was above 1480 K (1207 $^{\circ}\text{C}$, 2204 $^{\circ}\text{F}$). The weight of deposits increased by a factor of 30 when the gas temperature was increased to 1560 K (1287 $^{\circ}\text{C}$, 2348 $^{\circ}\text{F}$). Additional fly ash deposition studies are referenced in Murphy et al.

Figure 5(d) to (f) show that there would be a benefit to using glass-phase CMAS for the 1944 K burner case. In these cases, each of the particles was melted because partial melting as the particle temperatures stall at the melting point has been avoided. The plot for the particle preheated to 693 K (Figure 5(e)) showed a small benefit for the 30 and 40 μm particles. As with the crystalline particles, there was a small additional benefit to heating the duct to 1473 K (Figure 5(f)).

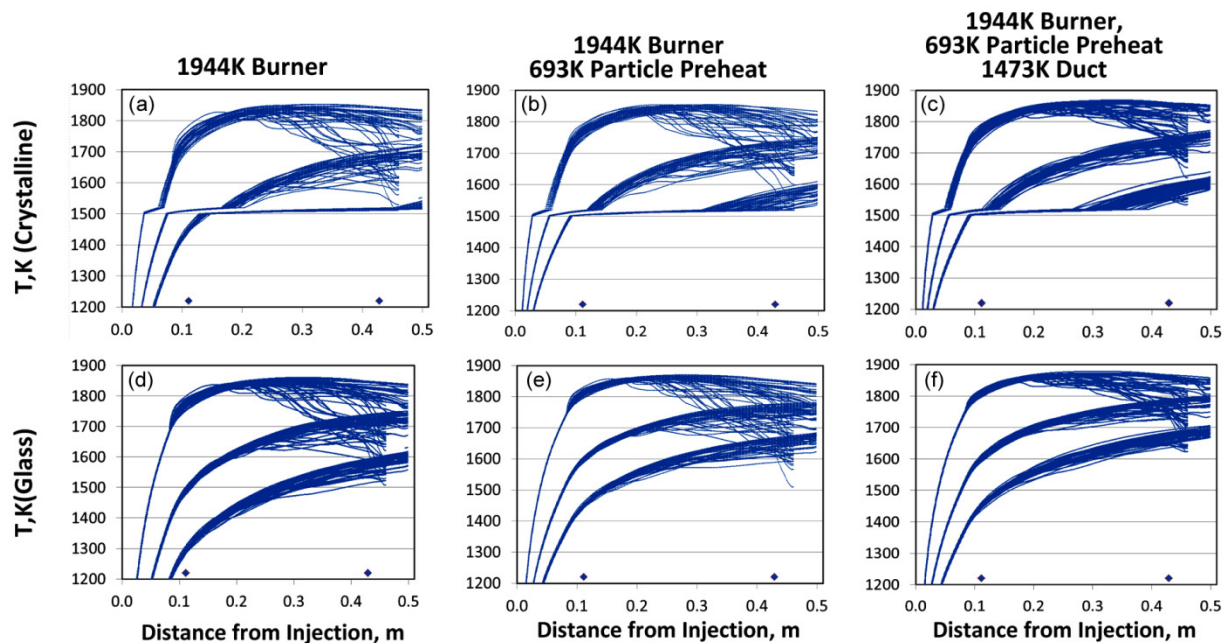


Figure 5.—Modeled particle temperature versus distance from injection for CMAS particles of diameter 20 μm (upper family of curves), 30 μm (middle family), or 40 μm (lower family) for 1944 K burner temperature and Mach 0.3 with and without particle preheating and duct heating. Diamond shaped symbols represent burner and duct exit locations, respectively.

It is not surprising that melting is favored by higher burner temperature and smaller particle size, and it is promising that the recent temperature measurements suggest that the higher temperature range of 1944 K may be appropriate. Also, it is promising to see that it should be possible to melt particles with reasonable sizes of at least 30 μm . The effect of Mach number was harder to predict. At the higher Mach number, somewhat higher gas-to-particle heat transfer would be associated with the somewhat higher burner pressure and somewhat higher gas velocity. The factors favoring improved particle heating at lower Mach number are the longer residence time and the higher static temperature of the gas. As discussed above, particle temperatures tend to approach the static temperature of the gas [Kuczmariski, 2011]. Given the same total temperature, higher gas velocity results in static temperatures that are lower than the total temperature by a factor of $\frac{1}{2}V^2/C_p$, where V is the gas velocity and C_p is the heat capacity of the gas.

The plots of particle velocities in Figure 6 represent 60 particle tracks from four adjacent injection locations. The faster of the particle tracks correspond to the 20 μm particles. The slower ones correspond to the 40 μm particles. The particles traveled at relatively low velocities within the burner, rapidly accelerated through the burner nozzle, then continued to increase in velocity, but at a lower rate, as they traveled through the duct. There was a small deceleration observed after exiting the duct just before striking the specimen. It may also be noted that the calculated maximum particle velocities resulting from Mach 0.5 versus 0.3 rig operation scaled by approximately the factor 5/3—the ratio of Mach numbers. The calculated maximum velocity at 1944 K scales to the velocity at 1644 K by approximately $(1944/1644)^{1/2}$ —the ratio of sonic velocities for each temperature.

The plots in Figure 7 show the static temperatures associated with each particle track. Figure 7(a) to (c) represent 1644 K burner temperature cases and Figure 7(d) to (f) represent 1944 K cases. In either case the static temperature was seen to be higher for Mach 0.3 than for Mach 0.5; i.e., Figure 7(b) versus (a) of Figure 7(e) versus (d). As expected, the static temperature within the burner in each case was close

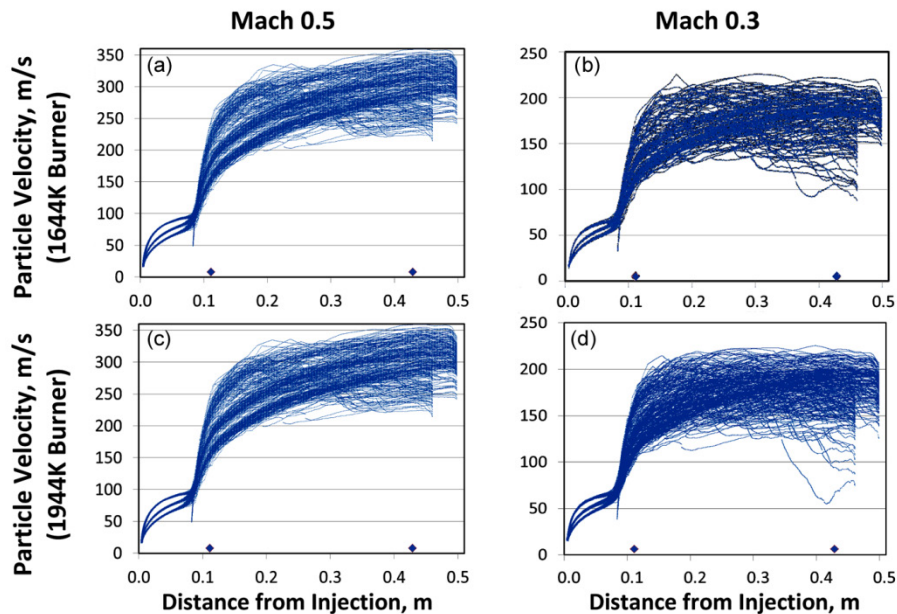


Figure 6.—Modeled particle velocity versus distance from injection for CMAS particles of diameter 20 μm (upper family of curves), 30 μm (middle family), or 40 μm (lower family) for 1644 or 1944 K burner temperature at Mach 0.5 or 0.3. Diamond shaped symbols represent burner and duct exit locations, respectively.

to the burner temperature due to the lower gas velocity. The static temperature dropped at the nozzle then rose somewhat as it entered the duct because of a temporary reduction in the gas velocity [Miller, 2011]. The static temperature dropped with increasing distance down the duct because the total temperature cooled off somewhat and the gas velocity was increasing. The maximum temperature at any distance down the duct is expected to occur at the centerline of the duct. Interestingly, when particles strike the duct wall, they briefly experience static temperatures that were presumably equal to the wall temperature. However, the particles did not remain at the cooler duct wall region long enough for their temperature to decrease. Therefore, as shown in Figure 3 to Figure 5, there was no drop in the temperature of particles after striking the duct wall. For the 1644 K cases, it is important to note that the static temperatures within the duct were not appreciably higher than the assumed melting range of 1500 to 1520 K, which helped explain why it was difficult to fully melt the particles in the 1644 K burner case.

Figure 7(c) and (f) represent cases where the temperature of the duct is fixed at 1473 K for burner temperatures of 1644 and 1944 K, respectively. Fixing the duct wall temperature at 1473 K also fixes the static temperatures at the duct wall to that temperature. Increasing the gas temperature at the wall increases the average temperature that the particles experience and the relative benefit of heating the duct wall to 1473 K will be greater for the 1644 K case than for the 1944 K case. That is, heating the duct is expected to be more beneficial at 1644 K and less so at 1944 K.

The right-most point in each plot of Figure 7 is a measure of the specimen temperature. Although the present study did not attempt to faithfully represent the heat transfer to the specimen, the results strongly suggest that a test configuration employing the aperture plate may not reach the desired high temperatures. This is because a significant portion of the heat content of the flame is discarded when the aperture plate is use. While the presence of the aperture helped clarify the figures in this paper, it appears likely that the aperture plate should not be used for the envisioned experiments. Recent experiments have shown that this is true and that care must be taken to manage the convective and radiative heat losses from the specimen so that maximum specimen temperature can be achieved.

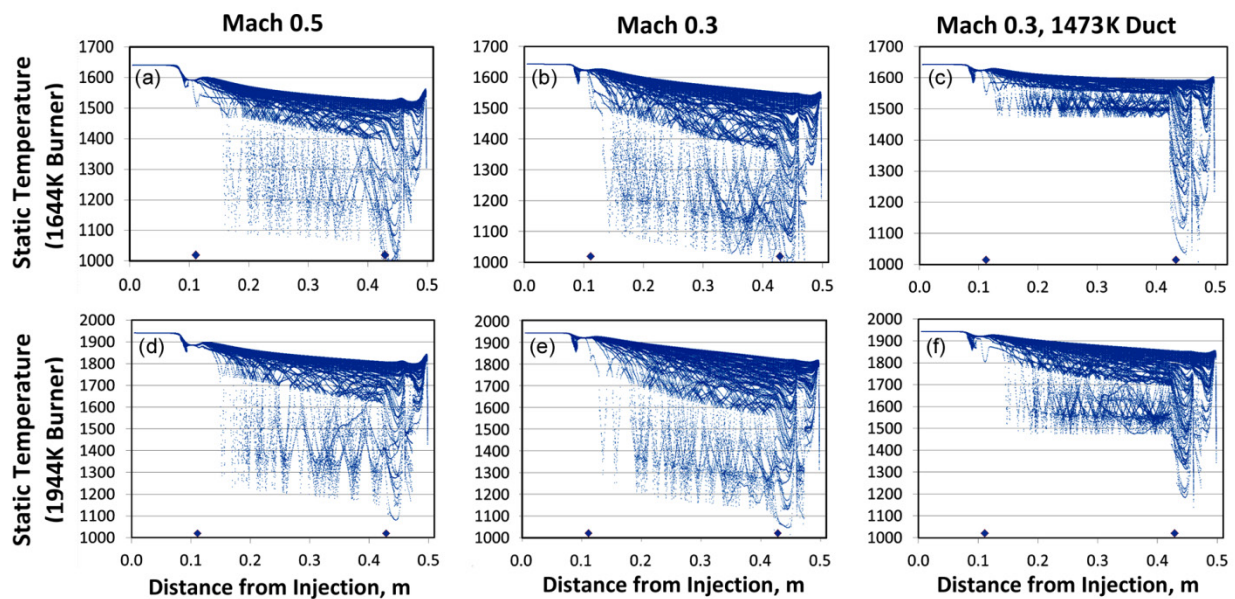


Figure 7.—Static temperature associated with the location of each particle track versus distance from injection for various combinations of burner temperature, Mach number, and duct heating. Particles striking the wall momentarily experience the low static temperatures at the wall. Diamond shaped symbols represent burner and duct exit locations, respectively.

The above discussion assumed that CMAS would not deposit within the duct. This was consistent with the experimental observation for fly ash [Laycock, 2013] when the duct was fabricated from a superalloy. The possibility of CMAS deposition was modeled for the cases described in Figure 5(f), Figure 6(d), and Figure 7(f). These models used 1944 K as the burner temperature, Mach 0.3, 693 K initial powder temperature, and 1200 K duct temperature while allowing each particle track striking the duct to be captured. The results was that about 1/3 of the particles were captured by the duct, another 1/3 were captured by the aperture plate, and the final 1/3 reached the specimen. The appearance of the figures was not greatly affected by the removal of particles by the duct except for Figure 7(f) where the particle tracks striking the 1473 K duct terminated at that temperature.

Discussion

The CFD analysis has demonstrated the potential feasibility of using an existing burner erosion rig for molten CMAS studies. While the modeled results are not necessarily expected to precisely describe the behavior of CMAS in the burner rig, the analysis has provided excellent insights into how to effectively operate the rigs to maximize particle melting and also how to best preprocess the CMAS.

Because of the primary importance of burner temperature, it is advisable to carefully characterize the essentially equivalent temperature of the isentropic core of the flame just downstream of the nozzle as well as the temperature at the duct exit. The simplest approach would be to measure using higher temperature-capable Type B thermocouples, and to apply corrections for heat losses from radiation and conduction down the lead wires.

The analysis shows that it will be advisable to maximize the residence time within the burner. For more complete melting, operating at Mach 0.3 would be preferred over Mach 0.5. Even lower Mach numbers could be considered, although the burner stability may not be adequate with Mach number less than 0.3 based on prior experience. It may be possible to increase residence time significantly by injecting the powder through a new port located further upstream in the burner. One disadvantage of Mach 0.3 operation is that the lower gas velocity would lead to lower heat transfer to the specimen. As a result, the specimen would come to somewhat lower temperature than would be possible operating at a higher Mach number. If the achievable maximum specimen temperatures are not as high as desired for the CMAS study, it is possible to increase the specimen temperature by placing a high reflectivity platinum mirror behind the specimen to reflect a significant portion of the heat loss due to radiation back onto the specimen. Also, the aperture whose presence was useful for visualizing the results above is expected to intercept an appreciable portion of the total heat content of the flame. Therefore, omitting the aperture will likely be necessary if maximum specimen temperature is to be achieved. A further benefit can be achieved using small specimen size, to minimize the fraction of the specimen that is not being heated by direct flame impingement. For solid particle erosion studies, flat specimens should generally be larger than the flame size. That requirement could likely be relaxed for CMAS corrosion studies. The possibility of independently heating the specimen, for example by small electric heaters, could also be examined.

Preheating the powder in the feed line has a relatively small beneficial effect, but in marginal situations it would be very easy and inexpensive to put into practice. Heating cables with the capability to bend around small diameter feed lines are available. The powder is currently injected using 20 m/s air flow. The powder is assumed to travel at 17.5 m/s for the modeling. Its residence time is expected to be sufficient for heating the gas and the powder over the available length of feed line.

The duct, which is currently fabricated from Schedule 40 Haynes 230 superalloy pipe, can be replaced with higher temperature capable Haynes 214 pipe. Since the temperature of the duct is expected to come to less than the 1473 K temperature capability of the alloy, the duct could be heated to that

temperature using a tube furnace; however, the benefit of heating the duct to 1473 K was found to be inversely proportional to the burner temperature. Therefore, if the burner temperature is 1944 K or higher, there may be minimal benefit from heating the duct unless deposition was observed within the duct. Insulating the duct is another alternative. The residence time could be increased by using a longer duct, which would require moving the burner further away from the exhaust duct. It seems likely that a longer duct may benefit even more from heating or insulating. Figure 1(b) shows that the duct entrance is currently air cooled and that a flange is welded to the pipe to keep the cooling air off of the burner nozzle. For melting CMAS, it may be desirable to use a simple uncooled straight pipe or one that is only marginally cooled at the entrance. However, if deposits are observed within the duct then heating could be considered.

In the unexpected event that the burner temperature is found to only be marginally hot enough or if sufficiently high specimen temperatures are not being achieved, the combustion air could possibly be preheated further or it could possibly be enriched with oxygen. According to modeling using the NASA thermodynamic equilibrium code [McBride, 2002], adding 10% oxygen to the preheated combustion air increases the adiabatic flame temperature by almost 100 K. A concern for rig durability would advise against excessive enrichment or excessive combustion air preheating.

If it was determined that larger particles were not melting completely, the size of the CMAS particles could be limited to 30 μm or even 20 μm . Glass phase CMAS could be ball milled and sieved to size. If the powder were in crystalline or even spray dried form, it could be fed one or more times through a plasma torch. That would spheroidize the powder and complete the reaction between the constituent oxides. The process of spheroidizing the CMAS powder may convert it fully, or at least partially, to a glass. Complete conversion to glass was observed with a plasma sprayed CMAS composition with a similar silica level to the composition being modeled for the present study, although it contained 0.5% K_2O [Bolelli, 2007]. As discussed above, glass phase powders are more difficult to heat up at first but that initial stage of heating occurs efficiently within the burner. There is a benefit to avoiding going through a heat of melting as the powder travels down the duct, since heating rates are lower at that location than they are within the burner.

After a satisfactory set of conditions had been established, the rig could be used for long-term deposition/corrosion studies to elucidate the response of environmental barrier coatings to CMAS attack.

The thermodynamic properties used for this study can be refined further through the use of a commercial software package such as CALPHAD. The software could be used to model more complicated CMAS-based compositions containing transition metal oxides such as iron or nickel oxide. Iron oxide is especially interesting because iron can take on different oxidation states that can be acidic or basic depending on whether the environment is oxidizing or reducing. Iron is a minor constituent of CMAS in aero applications and, of course, it is present in greater concentrations in slags. The effect of iron on CMAS melting would be of interest. There have been numerous attempts to model the melting, fluidity, or viscosity of slags in the literature, the simplest of which observe that melting or fluidity points are lowest when the acidic oxides are approximately equal in concentration to the basic oxides where iron is treated as ferric oxide in an oxidizing environment [Winegartner, 1975; Wang, 2013]. Understanding the effect of iron was beyond the scope of this study, but it should be possible using properties obtained from the software package. The thermodynamic properties of the gas may also be refined by using transport properties calculated using the chemical equilibrium code [McBride 2002]. After refined properties are obtained, the final rig design has been settled on, and temperatures have been characterized, a refined CFD model may be generated. The model can include the heating profile of the duct if a furnace is used.

Summary of Recommendations

Based on insights and understanding gained by the CFD modeling, the following recommendations may be offered for studies requiring more complete CMAS melting:

- Obtain more accurate burner temperature measurements using Type B thermocouple, heat transfer modeling, and silicon melting experiments.
- Operate the burner under Mach 0.3 conditions; possibly with somewhat higher combustion air preheating.
- Consider injecting powder through a new port located further upstream in the burner.
- Consider preheating the powder using heating cables wrapped around the feed line at least for cases where the resulting small additional final temperature would be beneficial.
- Change to a higher-temperature capable Haynes 214 superalloy pipe for the duct.
- Attempt to use the duct with no air cooling or minimal cooling at the duct entrance.
- Consider lengthening the duct by at least 50%.
- Measure the duct temperature and, assuming it is less than 1473 K, consider placing the duct within an electrically heated tube furnace or at least insulating the duct. Heating the duct may be helpful if CMAS is observed to deposit within the duct.
- If the burner rig is not sufficiently hot, consider possibly further preheating the cooling air or enriching the combustion air with 10% oxygen.
- Do not use the aperture plate so that maximum specimen temperatures may be obtained.
- Obtain -37 μm CMAS powder. If the powder was not in the glass phase, plasma spheroidize the micron powder to complete any chemical reactions and convert the powder to a glass.
- Sieve the powder to -30 μm , or -20 μm if required, to ensure complete melting.
- Develop long-term deposition/corrosion studies to elucidate the response of environmental coatings to CMAS attack.
- Use available thermodynamics software to refine the assumed thermodynamic properties, and then extend the analysis to more complicated compositions containing small amounts of transition metal oxides.
- Refine the CFD model after refining the thermodynamic properties and after characterizing the final rig design and refine gas transport properties using the chemical equilibrium code.

References

- ASTM (2010) D1857 / D1857M - 04(2010) Standard Test Method for Fusibility of Coal and Coke Ash, D05.21, Book of Standards Volume: 05.06, ASTM International, West Conshohocken, PA.
- Bolelli, G. (2007), L. Lusvardi, T. Manfredini, E. Parsini, and C. Siligardi, BAS, CMAS and CZAS Glass Coatings Deposited by Plasma Spraying. *Journal of the European Ceramic Society* 27, 16, 4575-4588.
- Chase Jr, M. W. (1998), NIST-JANAF Thermochemical Tables. American Chemical Society; American Institute of Physics for the National Institute of Standards and Technology. Woodbury, New York.
- Darolia, R (2007), B.A. Nagaraj, D.G. Konitzer, M.D. Gorman, and M. Fu. Layered Thermal Barrier Coatings Containing Lanthanide Series Oxides for Improved Resistance to CMAS Degradation, US Patent, US20070160859A1, Jan 6, 2006.
- Darolia, R. (2013). Thermal Barrier Coatings Technology: Critical Review, Progress Update, Remaining Challenges and Prospects, *International Materials Reviews*, March 2013.

- Ertuk, J. (1995) and J. McKelliget, Heat Transfer during Burner Rig Thermal Fatigue of Ceramic Matrix Composites. *Ceram Eng. Sci. Proc.*, 16, 4, 95-104
- Immarigeon, J-P (1997), V.R. Parameswaran, D. Chow, D.D. Morphy, P. Gougeon, M. Prystay, and C. Moreau, Evaluation of Thermal Barrier Coatings from Burner Rig Tests. Paper R-823 presented at AGARD SMP Meeting on Thermal Barrier Coatings, Aalborg, Denmark, October 15-16 1997.
- Kuczmariski, M. A. (2011), R.A. Miller, and D. Zhu. CFD-Guided Development of Test Rigs for Studying Erosion and Large-Particle Damage of Thermal Barrier Coatings. Modelling and Simulation in Engineering, 2011.
- Laycock, R.G. (2013), T.H. Fletcher, Time-Dependent Deposition Characteristics of Fine Coal Fly Ash in a Laboratory Gas Turbine Environment, *ASME Journal of Turbomachinery*, 135, 21003-1 thru 8.
- McBride, B.J. (2002), M. Zehe, and S. Gordon, NASA Glenn Coefficients for Calculating Thermodynamic Properties of Individual Species, NASA Technical Publication TP-2002-211556.
- Miller, R. A. (2011), M.A. Kuczmariski, and D. Zhu, Burner Rig with an Unattached Duct for Evaluating the Erosion Resistance of Thermal Barrier Coatings, NASA Technical Memorandum 2011-217008, June, 2011.
- Miller, R.A. (2013) and M. A. Kuczmariski, Burner Rig for Small Particle Erosion Testing of Thermal Barrier Coatings. Submitted to the *ASTM Journal of Testing and Evaluation*.
- Mills, K. C. (2011), L. Yuan, and R.T. Jones, Estimating the Physical Properties of Slags, *Journal of the Southern African Institute of Mining and Metallurgy*, 111, 649-658.
- Murphy, R.G. (2013), A.C. Nix, S.A. Lawson, D. Straub, and S.K. Beer, Proceedings of ASME Turbo Expo 2013, June 3-7, 2013, San Antonio TX, GT2013-94657.
- Okamoto, H (2013), Pt-Rh (Platinum-Rhodium), *Journal of Phase Equilibria and Diffusion*, 34, 2, 176-177.
- Vassilev, S. V. (1995), K. Kitano, S. Takeda, and T. Tsurue, Influence of Mineral and Chemical Composition of Coal Ashes on Their Fusibility, *Fuel Processing Technology*, 45(1): 27-51.
- Wang, P. (2013) and M Massoudi, Slag Behavior in Gasifiers. Part I: Influence of Coal Properties and Gasification Conditions, 2013, 6, 784-806.
- Winegartner, E.C. (1975) and B.T. Rhodes, An Empirical Study of the Relation of Chemical Properties to Ash Fusion Temperatures, *J Engineering and Power*, 97, 3, 395-405.

